Analyst

PAPER

Cite this: *Analyst*, 2015, **140**, 1265

# Sorting of human mesenchymal stem cells by applying optimally designed microfluidic chip filtration

Heekyung Jung,[a,b] Myung-Suk Chun*[b] and Mi-Sook Chang*[a]

Received 4th August 2014,
Accepted 14th December 2014

DOI: 10.1039/c4an01430h

www.rsc.org/analyst

Human bone marrow-derived mesenchymal stem cells (hMSCs) consist of heterogeneous subpopulations with different multipotent properties: small and large cells with high and low multipotency, respectively. Accordingly, sorting out a target subpopulation from the others is very important to increase the effectiveness of cell-based therapy. We performed flow-based sorting of hMSCs by using optimally designed microfluidic chips based on the hydrodynamic filtration (HDF) principle. The chip was designed with the parameters rigorously determined by the complete analysis of laminar flow for flow fraction and complicated networks of main and multi-branched channels for hMSCs sorting into three subpopulations: small (<25 μm), medium (25–40 μm), and large (>40 μm) cells. By focusing with a proper ratio between main and side flows, cells migrate toward the sidewall due to a virtual boundary of fluid layers and enter the branch channels. This opens the possibility of sorting stem cells rapidly without damage. Over 86% recovery was achieved for each population of cells with complete purity in small cells, but the sorting efficiency of cells is slightly lower than that of rigid model particles, due to the effect of cell deformation. Finally, we confirmed that our method could successfully fractionate the three subpopulations of hMSCs by analyzing the surface marker expressions of cells from each outlet.

## Introduction

Human bone marrow-derived mesenchymal stem cells (hMSCs) are considered as an ideal cell source for cell therapies to treat various intractable diseases due to their multipotent properties, low immunogenicity, and a lower risk of tumor formation than embryonic stem cells. The utilization and manipulation of hMSCs have been one of the most promising approaches in tissue engineering and regenerative medicine for the last decade.[1–3] However, hMSCs consist of heterogeneous subpopulations with different self-renewal capacities and multipotent properties. They have been classified into three distinct subpopulations based on morphological characteristics: small rapidly self-renewing (RS) cells, elongated, spindle-shaped (SS) cells, and slowly replicating, large, flattened (FL) cells.[4–6] Furthermore, small RS cells have been shown to possess the highest multipotency to differentiate into various cell types, while large FL cells are considered to be very early osteogenic progenitors with the subsequent loss of stem cell characteristics.[6] Thus, sorting these stem cells based on their size is important to increase the effectiveness of cell therapy.

Manipulation and sorting of cells cause great interest in biomedical applications, including in the fields of cell biology, clinical diagnostics, and oncology.[7–10] Purified cell samples with enhanced concentrations of interest are important in studying their biological and physical properties. For instance, many studies have dealt with the cell sorting and fractionation, *inter alia*, of the fluorescence activated cell sorter (FACS) and magnetic activated cell sorting (MACS). Although FACS can achieve high purity, it requires complicated and expensive instruments.[11] MACS is a high-efficiency process, but can only be run in a batch mode, as it has a problem of detaching cells from cell-bead complexes for subsequent utilization steps.[12]

Based on the benefits of microfluidics and microfabrications, recent studies that aim to innovatively manipulate particles and living cells have been reported.[13] The active separation is realized by using external fields, such as magnetophoresis, dielectrophoresis, and optical methods.[14–16] Instead of utilizing external forces, hydrodynamic effects combined with the fluid interaction with the microfluidic channel are capitalized upon to obtain passive separation based on the inertial force,[17,18] pinched flow,[19] and hydrodynamic filtration (HDF).[20–23] In the last decade, Seki and colleagues have devoted their efforts to separations of particles and cells by using a microfluidic chip with multiple branch channels

[a]*Laboratory of Cellular Neurobiology, Dept of Oral Anatomy, School of Dentistry & Dental Research Institute, Seoul National University, Jongno-gu, Seoul 110-749, Republic of Korea. E-mail: mschang@snu.ac.kr; Tel: +82-2-740-8628*
[b]*Complex Fluids Laboratory, National Agenda Research Division, Korea Institute of Science and Technology (KIST), Seongbuk-gu, Seoul 136-791, Republic of Korea. E-mail: mschun@kist.re.kr; Tel: +82-2-958-5363*

based on the HDF principle.[20–23] Here, a continuous flow with suspended samples enters the main channel and the selective extraction of streamlines is controlled by the flow fraction at each branch for particle alignment and separation. Only the stream near the sidewall enters the branches, with the amount of fluid leaving the main channel being determined by the flow distribution related to the hydraulic flow resistances in the channel networks. They performed separations for various types of cells: *e.g.*, liver cells, white blood cells from red blood cells, JM cells (human T-lymphocyte cell line), and HeLa cells (human epithelial tumor cell line). It is emphasized that HDF is advantageous for continuous operation without using chemicals and does not need chemical treatment or magnetic or electric fields which may affect cells.[20,22,23]

In this study, microfluidic chip filtration is applied for the hMSCs sorting, which has not been reported yet, even though the heterogeneous nature of hMSCs causes an actual limitation for cell therapy. We solve the pressure-driven laminar flow in microfluidic networks, since its understanding is important in chip design, but it has very simply been treated in the previous studies without in-depth consideration. Trimodal separation is performed in view of the classification of hMSC with three subpopulations, where multiple branches are effective in removing excess fluid gradually, causing the line-up of cells along the main channel walls. A different routing design of channels was used, where slanted branch channels with an angle of 60 degrees are in parallel to the direction of the side channel to effectively perform the selective focusing. By focusing with a proper ratio between main and side flow rates, cells were diverted into the side branch by side flow. In order to quantify the sorting efficiency of our designed chip, we estimate the recovery of different outlets for each population and the purity of each population at different outlets. Our results confirmed the validity of microfluidic chip filtration, suggesting its potential application to the rapid and precise fractionation of hMSCs with high multipotency.

## Flow fraction in rectangular microchannel

The principle of flow-based HDF is similar to conventional crossflow filtration which utilizes many capillary branches perpendicular to the main flow. The role of the branches in HDF lies in removing carrier fluid and forcing particles to move closer to the sidewalls of the main channel, which is called particle focusing.[7,20] In Fig. 1, particle suspension represented as the complex fluid is introduced into the main channel, displaying a gray color. The medium of suspension supplied into the side channel forms a side flow of simple fluid, which effectively enhances the focusing. If the strength of the flow fraction is very weak, the particles with radii larger than the width of the stream will not enter the branches. The virtual boundary of the fluid layer in the gray-colored region is termed as the cut-off width $W_C$ that will be diverted into the branches. Here, fully-developed laminar flows apply for a main channel that is

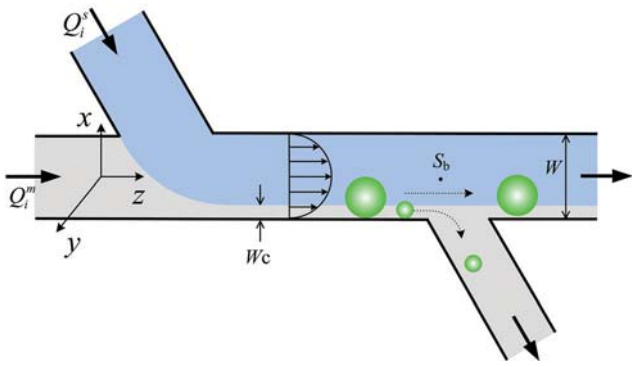


**Fig. 1** Schematic of the flow fraction and HDF of particles in microchannel with a branch, on the basis of the cut-off width of fully-developed flow stream.

straight and long enough as $L/r_h \gg 1$ and $L/r_h \gg \mathrm{Re}$, where $L$ is the channel length, $r_h$ is the equivalent hydraulic radius, and Re means Reynolds number. The precise control of the flow into branches decides flow lanes, as illustrated in Fig. 1, allowing small particles located in the gray-colored region to be separated from the medium but not allowing large particles to be separated as these have a hydrodynamic center outside the region.

In order to precisely predict the fractioned boundary width, we take into account the 3-dimensional flow profile at the rectangular cross-section with any aspect ratios and then derive the flow ratio between each incoming or outgoing stream. Considering the velocity field for a Newtonian fluid at the steady state laminar flow $\mu\nabla^2\boldsymbol{v} = \nabla P$, the basic equation for rectangular microchannel with the width $W$ and the height $H$ is given by

$$\frac{\partial^2 v_z}{\partial x^2} + \frac{\partial^2 v_z}{\partial y^2} = \frac{1}{\mu}\frac{\mathrm{d}P}{\mathrm{d}z}. \tag{1}$$

Here, $v_z$ is the streamwise axial velocity in the $z$-direction, $P$ is the pressure drop applied along the channel length, and $\mu$ is the fluid viscosity. The analytical solution for $v$ with no-slip boundary condition is available as[24]

$$v_z(x,y) = \frac{4H^2}{\pi^3\mu}\frac{\Delta P}{L}\sum_{n=\mathrm{odd}}^{\infty}\frac{1}{n^3}\left[1 - \frac{\cosh(n\pi x/H)}{\cosh(n\pi W/2H)}\right]\sin(n\pi y/H). \tag{2}$$

The streamwise average velocity can be expressed by integrating eqn (2) over the height along the $y$-direction,

$$\bar{v}_z(x) = \frac{1}{H}\int_0^H v_z(x,y)\mathrm{d}y = \frac{8H^2}{\pi^4\mu}\frac{\Delta P}{L}\sum_{n=\mathrm{odd}}^{\infty}\frac{1}{n^4}\left[1 - \frac{\cosh(n\pi x/H)}{\cosh(n\pi W/2H)}\right]. \tag{3}$$

Further, the average velocity in the channel is obtained by integrating eqn (3) along the spanwise $x$-direction,

$$\begin{aligned}\bar{v}_z &= \frac{2}{W}\int_0^{W/2}\bar{v}_z(x)\mathrm{d}x \\ &= \frac{H^2}{12\mu}\frac{\Delta P}{L}\left[1 - \frac{192}{\pi^5}\frac{H}{W}\sum_{n=\mathrm{odd}}^{\infty}\frac{1}{n^5}\tanh(n\pi W/2H)\right].\end{aligned} \tag{4}$$

where $\sum_{n=\text{odd}}^{\infty} n^{-4}$ equals to $\pi^4/96$ by the Riemann zeta function. Then, the volumetric flow rate $Q$ is described by the hydraulic resistance $R$ such that

$$Q = \frac{WH^3}{12\mu}\frac{\Delta P}{L}\left[1 - \frac{192}{\pi^5}\frac{H}{W}\sum_{n=\text{odd}}^{\infty}\frac{1}{n^5}\tanh(n\pi W/2H)\right] = \frac{\Delta p}{R}. \quad (5)$$

Next, we consider the fractional flow rate $Q_X$ for the focused stream in the range $-X \le x \le 0$ (or $0 \le x \le X$, due to symmetry) with $X = W/2 - W_C$, derived by

$$\begin{aligned} Q_X &= \int_0^X \int_0^H v_z(x,y)\mathrm{d}y\mathrm{d}x \\ &= \frac{WH^3}{24\mu}\frac{\Delta P}{L}\left[\frac{2}{W}X - \frac{192}{\pi^5}\frac{H}{W}\sum_{n=\text{odd}}^{\infty}\frac{1}{n^5}\frac{\sinh(n\pi X/H)}{\cosh(n\pi W/2H)}\right]. \end{aligned} \quad (6)$$

In Fig. 1, the partial volumes of the parabolic velocity profile are proportional to the flow rates of each stream fractioned by the virtual boundary. Here, we define the ratio of the flow fraction $\xi$ in the forefront of the branch point as the ratio of the volumetric flow rate $Q_i^m$ to $Q_i^s$. It can be determined by identifying $Q_i^m + Q_i^s = Q$ and $Q_i^m + Q_X = Q/2$, given by

$$\xi \equiv Q_i^m/Q_i^s = (Q - 2Q_X)/(Q + 2Q_X). \quad (7)$$

By applying $\Gamma_1 = \tanh(n\pi W/2H)$, $\Gamma_2 = \cosh(n\pi W/2H)$, and $\Gamma_3 = \sinh(n\pi X/H)$, eqn (7) becomes a general formula

$$\xi \equiv \frac{Q_i^m}{Q_i^s} = \frac{1 - 2X/W - (192/\pi^5)(H/W)\sum_{n=\text{odd}}^{\infty}[n^{-5}(\Gamma_1 - \Gamma_3/\Gamma_2)]}{1 + 2X/W - (192/\pi^5)(H/W)\sum_{n=\text{odd}}^{\infty}[n^{-5}(\Gamma_1 + \Gamma_3/\Gamma_2)]}. \quad (8)$$

We point out that this proposed model imposes no limitations on the channel aspect ratio $H/W$ and $W_C$. Simple expression is only valid in the specific cases of $H/W$. If $H/W > 1$, the ratio of flow fraction $\xi$ can simply be estimated from the ratio of the partial areas of parabola based on the 2-dimensional flow profile, such that $W_C^2(3W - 2W_C)/(W - W_C)^2(W + 2W_C)$.

## Chip design with channel networks for HDF

In order to sort out three populations from the hMSC, we designed the microfluidic chip containing three outlets to achieve the trimodal separation, as shown in Fig. 2a. Particles of certain size can escape from the main channel at a specific branch where its ratio of the flow fraction is optimized for the right particle size. From the condition for steady state flow ($L/r_h \gg \mathrm{Re}$), the parabolic velocity profile starts to form at a distance of approximately $\mathrm{Re}(2r_h)$ from the node of main and side channels. In view of the basic concept of Taylor–Aris dispersion, convection happens much faster than diffusion for high Péclet numbers ($>L/r_h$), thus the mixing of the two streams is quite slow.[25] After this distance, the streamline becomes parallel to the main channel. The branch point $S_b$ shown in Fig. 1 indicates that the laminar flow stream is divided into two streams: one is toward a following main channel and the other is toward a branch channel. There exist multiple branch points in Fig. 2b, such that eqn (8) becomes as follows, at the $j$th branch point $S_j$

$$\left.\frac{Q^b}{Q^m}\right|_{S_j} = \frac{1 - 2X/W - (192/\pi^5)(H/W)\sum_{n=\text{odd}}^{\infty}[n^{-5}(\Gamma_1 - \Gamma_3/\Gamma_2)]}{1 + 2X/W - (192/\pi^5)(H/W)\sum_{n=\text{odd}}^{\infty}[n^{-5}(\Gamma_1 + \Gamma_3/\Gamma_2)]}. \quad (9)$$

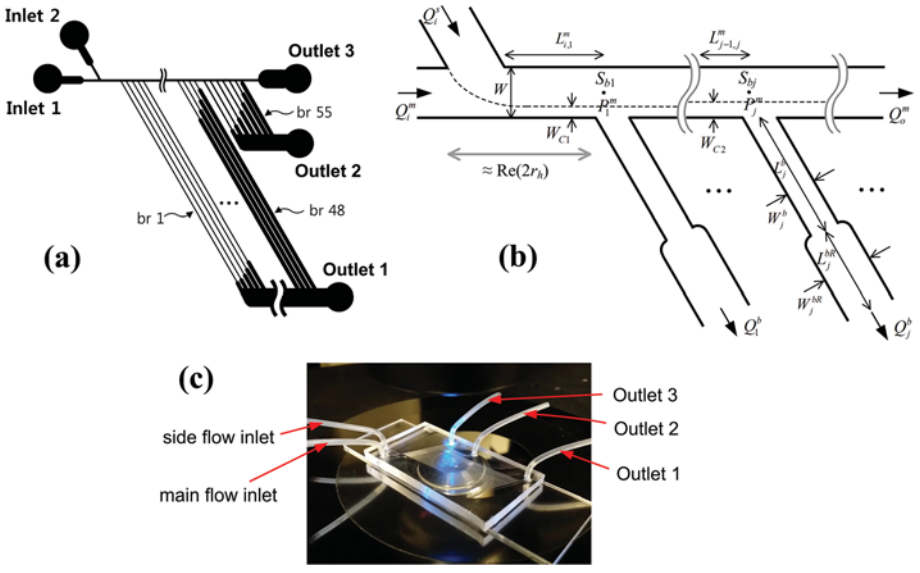


Fig. 2 (a) HDF microfluidic chip for sorting of particles and hMSCs, (b) multi-channel network for analysis and design, and (c) microfluidic chip used in this study, where the number of branch channels is 55 and the total length of the main channel is 16 mm.

Here, the finite number of terms required for sufficient accuracy depends on $H/W$ and $W_C$, mostly choosing the number of terms less than 4 (*i.e.*, $n$ = 1, 3, 5).

From eqn (5) with rapidly converging sums, the flow rate at the main channel between branch point $j-1$ and $j$ can be given as

$$Q^{m}_{j-1,j} \equiv \frac{\Delta P^{m}_{j-1,j}}{R^{m}_{j-1,j}} = \frac{WH^3}{12\mu}\frac{\Delta P^{m}_{j-1,j}}{L^{m}_{j-1,j}}\left[1-\frac{192}{\pi^5}\frac{H}{W}\tanh(\pi W/2H)\right]. \quad (10)$$

Since the corresponding flow rate $Q^{m}_{j-1,j}$ is represented by subtracting output flows at branches from 1st to $(j-1)$th from the total input flow $Q$, the pressure drop at the corresponding interval is estimated as

$$\Delta P^{m}_{j-1,j} = R^{m}_{j-1,j}\left(Q-\sum_{1}^{j-1}Q^{b}_{j}\right). \quad (11)$$

The 48 first channels and the 7 second channels branch off from the main channel and are connected to outlet 1 and outlet 2, respectively, where the main channel connects inlet 1 and outlet 3 with an invariant width.

The design of multiple branches is responsible for aligning against sidewalls and concentrating the particles by fluid removal, providing selectivity enhancement. All branches are located in parallel and slanted to the main channel with an angle of 60 degrees, which is the same directional angle to the side channel. This geometry has been adopted based on our preliminary study, identifying that slant branches provide better efficiency rather than perpendicular configurations. Branch channels are designed to consist of narrow and wide segments that make the total lengths of the channels uniform by adjusting their hydraulic resistances to specific values. Thus, the flow rate at the $j$th branch channel is given by

$$Q^{b}_{j} \equiv \frac{\Delta P^{b}_{j}}{R^{b}_{j}+R^{bR}_{j}} \quad (12)$$

where the hydraulic resistances for each section are arranged in series, expressed as

$$R^{b}_{j} = \frac{12\mu L^{b}_{j}}{W^{b}_{j}H^3}\left[1-\frac{192}{\pi^5}\frac{H}{W^{b}_{j}}\tanh\left(\pi W^{b}_{j}/2H\right)\right]^{-1}, \quad (13)$$

$$R^{bR}_{j} = \frac{12\mu L^{bR}_{j}}{W^{bR}_{j}H^3}\left[1-\frac{192}{\pi^5}\frac{H}{W^{bR}_{j}}\tanh\left(\pi W^{bR}_{j}/2H\right)\right]^{-1}. \quad (14)$$

We describe the detailed procedures of the chip design, by considering Fig. 2b. The particles with the hydrodynamic center less than a $W_C$ for the target population are expected to enter the branch channel, which allows sorting out. We set the heights and the widths of main as well as branch channels, total lengths of main and branch channels, and inter-distances between each branch channel. Table 1 summarizes all chip dimensions and their values.

Objective parameters for careful tuning of the design are each length of individual branch channels and the length between the last branch and outlet 3. The pressure drops between inlet and every outlet point are set to equal on the ground that the main and all branch channels are open to the atmosphere, yielding

$$\Delta P_{i,1} = \cdots = \Delta P_{i,j} = \cdots = \Delta P_{i,O3}. \quad (15)$$

Again, note that the pressure drop is basically described as the product of the flow rate and hydraulic resistance. From eqn (9)–(15), $\Delta P_{i,1}$ is first calculated for the initial guess of $L^{b}_{1}$, and then it is plugged into the repeat step of computation for $L^{b}_{j}$ by an iteration scheme on the condition of $\Delta P_{i,1} = \Delta P_{i,j}$ in the multiple branches. Sufficient minimum error is obtained by applying the nonlinear regression with the least sum of squares method based on a generalized reduced gradient (GRG) scheme.[26] Similarly, the length between the last branch and outlet 3 ($L^{m}_{55,O3}$) can be determined by an iteration scheme on the condition of $\Delta P_{i,1} = \Delta P_{i,O3}$.

**Table 1** Design parameters and values

| Channel | Dimension | | Notation | Values (μm) |
|---|---|---|---|---|
| Main | Height | | $H$ | 65 |
| | Width | | $W$ | 90 |
| | Length | | $L^{m}_{i,1}$ | 440 |
| | | | $L^{m}_{j-1,j}$ ($j$ = 1–48) | 280 |
| | | | $L^{m}_{j-1,j}$ ($j$ = 49–55) | 280 |
| | | | $L^{m}_{55,O3}$ | 1140 |
| | Cut-off | | $W_{C1}$ | 12.5 |
| | | | $W_{C2}$ | 20 |
| Branch | Height | | $H$ | 65 |
| | Total length | | $L^{bT}_{j}$ ($j$ = 1–48) | 3000 |
| | | | $L^{bT}_{j}$ ($j$ = 49–55) | 1000 |
| | Width | Narrow section | $W^{b}_{j}$ ($j$ = 1–48) | 54 |
| | | | $W^{b}_{j}$ ($j$ = 49–55) | 75 |
| | | Wide section | $W^{bR}_{j}$ ($j$ = 1–48) | 90 |
| | | | $W^{bR}_{j}$ ($j$ = 49–55) | 105 |
| | Length | Narrow section | $L^{b}_{j}$ | To be computed |
| | | Wide section | $L^{bR}_{j}$ | To be computed |

# Experimental

### Microfluidic chip and operation

After determining all values of channel dimension, we fabricated the polydimethylsiloxane (PDMS)/glass microfluidic chips by means of the standard soft lithography.[27] Channel design was performed with AutoCAD-2009 (Autodesk Inc.) and the photomask was prepared for the master mold on a silicon wafer. To create the master mold, the photolithography was employed with the negative photoresist (PR) SU-8 2050 (Microchem, MA) which coated onto the cleaned wafer by spinning. After UV patterning by the mask on the PR for 10 s with the mask aligner, the post exposure bake was carefully performed and then the unexposed PR was removed by dissolving with the SU-8 developer (Microchem, MA). To make a replica, the mixture of base and curing agent of the PDMS (Sylgard 184, Dow Corning, MI) in a volume ratio of 10 : 1 poured on the master mold was sufficiently degassed, and then cured at 80 °C for at least 1 h. The peeled PDMS replica was punched to generate holes for inlets and outlets and bonded to a slide glass using an $O_2$ plasma generator (CUTE-1MP, FemtoScience, Korea), following the post-bake. As shown in Fig. 2c, Teflon tubing (ID: 0.8 mm, OD: 1.5 mm) was connected to each reservoir of inlets and outlets.

The sample suspension was introduced into the main channel through the inlet 1 using a syringe pump (Pump 11 Elite-Nanomite, Harvard Apparatus, MA), and the medium fluid was injected into the side channel through the inlet 2 by another pump (KDS-200, KD Scientific, MA). The microfluidic chip was positioned on an inverted microscope (Eclipse Ti-E, NiKon, Japan) with a 10× objective (*cf.*, NA of 0.3, focal depth 2.7 μm) to allow monitoring and imaging. Streak images were taken by a digital 5 M pixel sCMOS camera (Zyla, monochrome cooled, ANDOR, UK) at an exposure time of 300 ms with NIS-Elements software, and the cell deformation was observed by an ultra high-speed CMOS camera (FastCam SA1.1, Photron, Japan) with $10^4$ frames $s^{-1}$ and a $15\,000^{-1}$ s exposure time. All sorting data obtained at least 3 times were analyzed by the ImageJ (NIH, MD). To observe the focusing with particle streaks, bidisperse particle suspension was prepared by fluorescent polystyrene latex (Thermo Fisher Scientific Inc., MA) of 15 and 39 μm in diameter $d_p$ dispersed in 0.2% (w/v) Triton X-100.

### The hMSC preparations

Adult bone marrow-derived hMSCs were purchased from Cambrex (MD, USA). hMSCs were cultured in Dulbecco's modified Eagle's medium (DMEM)-low glucose (WelGENE, Korea) containing 10% fetal bovine serum (FBS; Gibco, CA, USA) at 37 °C with 5% $CO_2$. The viability of cells was checked with trypan blue. We captured images of the cells in both cultured and suspended states and then analyzed them by the ImageJ. It is reasonably assumed that the cell dimension can be quantified by a 2-dimensional ellipsoid with major axis $L_l$ and minor axis $L_s$.

Fig. 3a shows the correlations between the longest length ($L_l$) and the area of cells at the cultured state, where our results are compared to the literature data. In view of the size-dependent properties of hMSCs, sorting out the target cells allows the differentiation efficiency to improve. Note that the size distribution in the suspended state is meaningful information for the microfluidic chip filtration. In Fig. 3b, the equivalent diameter $d$ ($= \sqrt{L_l L_s}$) of our hMSCs ranges from 16 to 62 μm with an average ± SE (standard error) of 26.1 ± 2.1 μm. We set their sizes into three groups: small (<25 μm), medium (25–40 μm), and large (>40 μm) one. The corresponding cumulative populations are estimated as 42, 47, and 11%.

The changes of flow fraction with different total flow rates and ratios of incoming streams between side and main flows were observed by introducing 0.2% (w/v) Triton X-100 and trypan blue into the main channel and side channel inlets, respectively. To take the streak images of cells in the microchannel, hMSCs expressing green fluorescent protein (GFP-hMSCs) previously generated by our research group were loaded into the chip.[28] In cell sorting, hMSCs were suspended at a concentration of $1 \times 10^5$ cells $mL^{-1}$ in DMEM, and injected into the main channel using a syringe pump. After the sorting experiment, the separated hMSCs were recovered from each outlet, and their numbers were counted to evaluate the sorting efficiency by analyzing cell images.

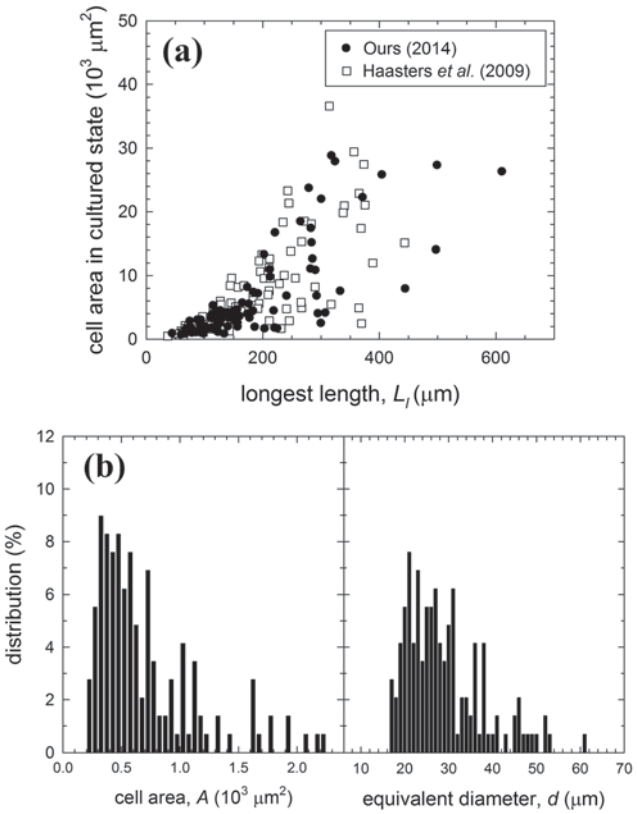


Fig. 3 (a) Relationship between the major axis and the 2-dimensional area of hMSCs in the cultured state compared with previously published data, and (b) distribution of suspended hMSCs based on 2-dimensional area and its equivalent diameter.

After sorting of hMSCs based on the size, we analyzed their surface marker expression at the single cell level using immunocytochemistry. The hMSCs collected from each outlet were seeded on the coverglass and cultured for 48 h. Then, cells were fixed with 4% paraformaldehyde, permeabilized, and blocked with 0.2% Triton X-100 and 5% normal goat serum in phosphate-buffered saline (PBS) for 1 h. Cells were incubated overnight at 4 °C with the following primary antibodies: mouse monoclonal (anti-CD73, 1 : 500; Invitrogen, CA, USA) and rabbit polyclonal (anti-CD90, 1 : 500 and anti-CD105, 1 : 500; Abcam, Cambridge, UK). After washing with PBS, cells were incubated with the following secondary antibodies: Alexa Fluor 546 anti-mouse IgG and Alexa Fluor 488 anti-rabbit IgG (Invitrogen, CA, USA). Cells were counterstained with 4,6-diamidino-2-phenylindole (DAPI, Santa Cruz Biotechnology, CA, USA) for nuclear staining. Cells were coverslipped with mounting medium (Dako, Glostrup, Denmark), and the images of immunopositive cells were captured using a laser-scanning confocal microscope (LSM700, Carl Zeiss, Germany).

## Results and discussion

### Side flow effect on focusing

The boundary width at the fully-developed flow region is determined by the ratio between side flow and main flow. It can be obtained from the microscope images and virtually corresponds to the cut-off width $W_C$ involved in eqn (8). In Fig. 4a, as the total flow rate $Q$ ($= Q_i^m + Q_i^s$) increases, $W_C$ decreases and becomes almost constant for the flow ratio $Q_s/Q_m < 6$. $W_C$ decreases with increasing $Q_s/Q_m$, indicating the higher focusing on the sidewall of the main channel. The flow ratio dependence on $W_C$ becomes weaker with decreasing total flow rate. For sorting out small hMSCs, the target value of $W_C$ is 12.5 μm for 48 branches connected to outlet 1, expecting that cells with $d < 2W_C$ would be removed through the branch channels. Based on our preliminary experiments, we applied total flow rate $Q$ of 30 μL min$^{-1}$, where the flow field at the initial fully-developed region of the main channel has an average velocity of 8.5 cm s$^{-1}$, Re of 6.45, and nominal wall shear rate of 8170 s$^{-1}$. The results in Fig. 4a show that the flow ratio $Q_s/Q_m$ of 6 is suitable for $Q$ of 30 μL min$^{-1}$. Fig. 4b verifies that our flow condition is effective to obtain the focusing and resultant sorting by HDF, showing that a large particle of 39 μm ($>2W_C$) passes along the main channel, whereas a small particle of 15 μm ($<2W_C$) flows into the branch channel. As a result, latex particles of 15 μm diameter would be recovered from outlet 1, and those of 39 μm diameter would be expected to be collected from outlets 2 and 3.

For the HDF chip used in this study, the ratio of flow distribution was computed as 91.5% at outlet 1, 5.3% at outlet 2, and 3.2% at outlet 3, regardless of $Q$. These ratios have been compared with the ratios obtained from measurements with $Q$ = 5, 30, and 100 μL min$^{-1}$. The discrepancy between prediction and experimental results is estimated less than 6.5% of prediction for 30 and 100 μL min$^{-1}$. This low discrepancy,

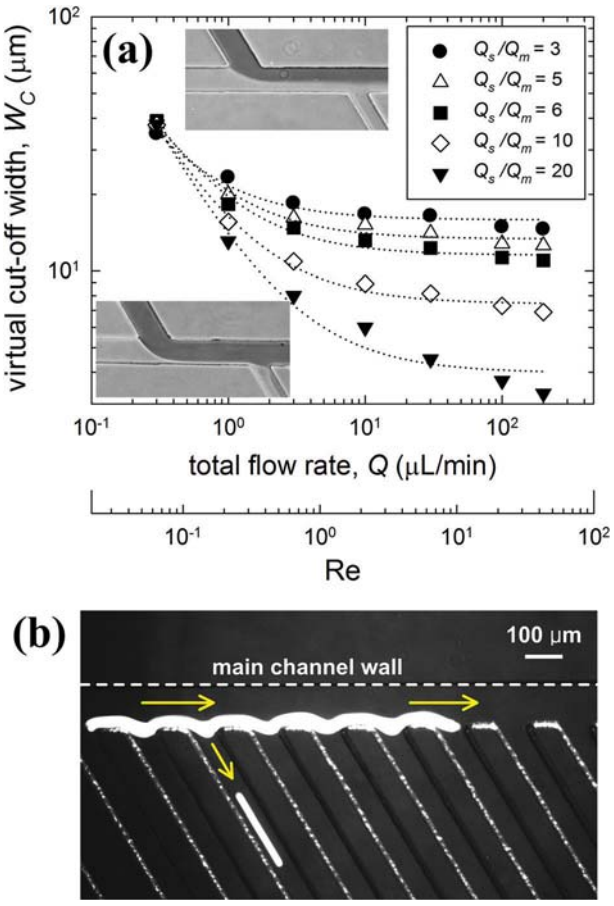


Fig. 4 (a) Virtual cut-off widths with variations of $Q$ and $Q_s/Q_m$, which are determined from the fully-developed region between the main/side channel node and the first branch point. Microscope images show flow lanes by weak focusing for $Q_s/Q_m$ = 6 and $Q$ = 0.3 μL min$^{-1}$ (upper) and strong focusing for $Q_s/Q_m$ = 20 and $Q$ = 100 μL min$^{-1}$ (lower). (b) Streak images of large particle (39 μm) flowing in the main channel and small one (15 μm) flowing in the branch channel, which were taken at the region between 4th and 12th branch points.

which may result from the actual dimension of fabricated channels deviating slightly from the design values, can verify the reliability of our chip design. However, lower $Q$ of 5 μL min$^{-1}$ results in high discrepancy in the range 20–28%, where the error in outlet 3 should be noted.

### Sorting of bidisperse spherical particles

The validity of our channel design was examined by sorting out model rigid particles of latex beads bidispersed with equivalent number concentrations. The recovery and purity can be estimated by the analysis of the number of particles collected from each outlet, which are used to access sorting efficiency or separation performance. The recovery is defined as the ratio of the number of target particles collected from a particular outlet to the total number of target particles in the sample collected from all outlets. The purity is represented as the ratio of the number of target particles to the total particle number in the collected sample at each outlet.

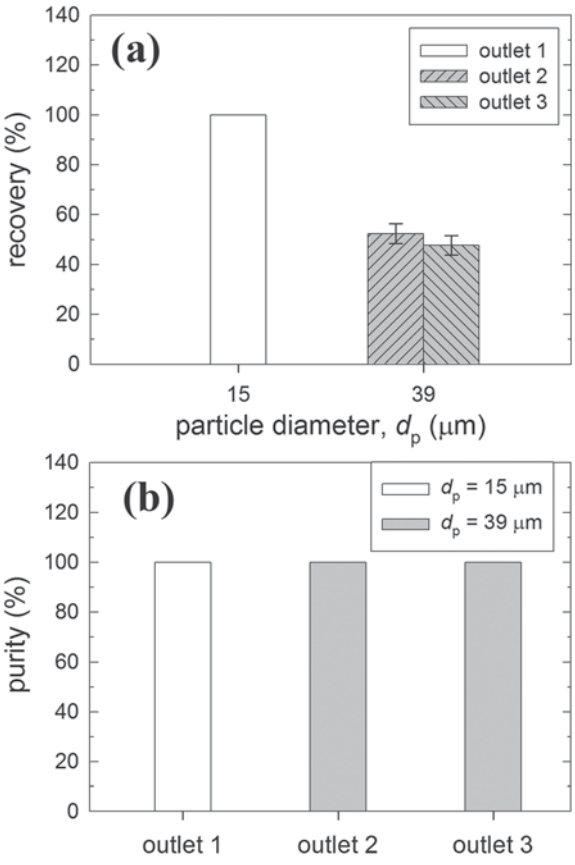


**Fig. 5** Sorting results for model latex particles with (a) purity at each outlet and (b) recovery distribution of particles according to outlet. Each value shows the mean ± SE from three independent experiments.

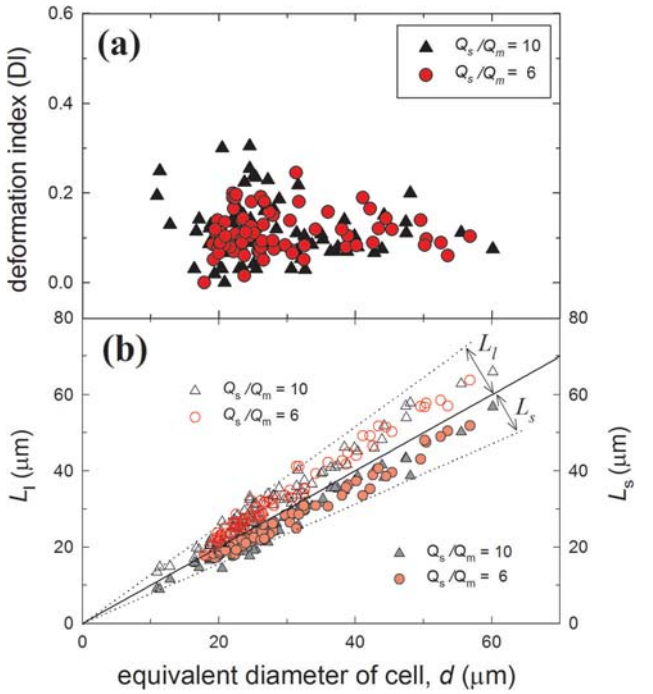


**Fig. 6** (a) Deformability changes of size-distributed hMSCs with different ratios of side to main flow, and (b) corresponding changes of major and minor axes, where $Q$ = 30 μL min$^{-1}$ and the average DIs are 0.114 and 0.110 for $Q_s/Q_m$ = 10 and 6, respectively.

In Fig. 5, the cut-off widths were given as 12.5 μm (= $W_{C1}$) for outlet 1 and 20 μm (= $W_{C2}$) for outlets 2 and 3. It is evident that, if the particle radius is larger than $W_C$, it flows through a main channel. On the basis of this condition, small (15 μm) particles were collected from only outlet 1 with 100% recovery, and large (39 μm) particles were distributed over outlets 2 and 3 with 100% recovery in total. Thus, both particles have the purity of 100% at each outlet, allowing perfect sorting efficiency.

### Sorting of hMSC subpopulations

We checked deformation behavior of hMSCs in flow field. In Fig. 6a, the deformation index DI (= $(L_l - L_s)/(L_l + L_s)$) becomes zero for the perfect spherical cell and unity for the infinitely deformed cell. The DI for higher values of $Q_s/Q_m$ results in a larger average value with wide variations. As shown in Fig. 6b, results of cell deformation at $Q$ = 30 μL min$^{-1}$ under higher side flow effect present that the $L_s$ value becomes shorter and the $L_l$ value becomes longer than the diameter of the undeformed spherical cell. This means spherical cells deform and become an ellipsoidal shape under the flow condition of shear field applied in the present study, but its deformability is clearly weak compared to the general case of extensional flow.

Fig. 7a shows the microscopic views of hMSCs before separation and collected from each outlet. For over 100 collected cells, the average size of cells was 17.2 ± 5.3 μm in outlet 1 and 28.8 ± 5.4 μm in outlet 2. In contrast, the range of large cell sizes collected from outlet 3 (*cf.*, 52 ± 13 μm) was more widely distributed than those from the other outlets, partly due to cell aggregations. Since the cell suspensions were introduced into the chip with $Q$ = 30 μL min$^{-1}$, it took 10 min to process 0.3 mL of a sample containing about $10^5$ hMSCs. The viability was 97 ± 0.5, 92 ± 0.8, and 90 ± 3.5% for the hMSCs sorted from outlets 1, 2, and 3, respectively, comparable to the results for liver cells previously reported.[22] Furthermore, on the basis of doubling time measurement, we have found that the small cells collected from outlet 1 grow faster than the others (*cf.*, 57.4, 69.1, and 100.9 h for each cell), as presented in Fig. 7b. Here, the doubling time $t_D$ can be calculated as $t_D = t[\ln 2/\ln(N_f/N_b)]$, with the cell number at the beginning of the incubation time $N_b$ and the one at the end of the incubation time $N_f$.

In order to quantify the sorting efficiency of hMSCs consisting of three subpopulations, we evaluated the recovery according to the size and purity at three outlets, as provided in Fig. 7c and d. Main collections of small (<25 μm), medium (25–40 μm), and large (>40 μm) cells occur from outlets 1, 2, and 3 with a recovery of *ca.* 94%, 87%, and 86%, respectively. Populations of small, medium, and large cells are collected in the purity of 100%, 81%, and 87% from outlets 1, 2, and 3, respectively. In the case of cells, the purity obtained from label-free microfluidic techniques can be found ranging about 60 to 99%. Our results remark that sorting out small as well as

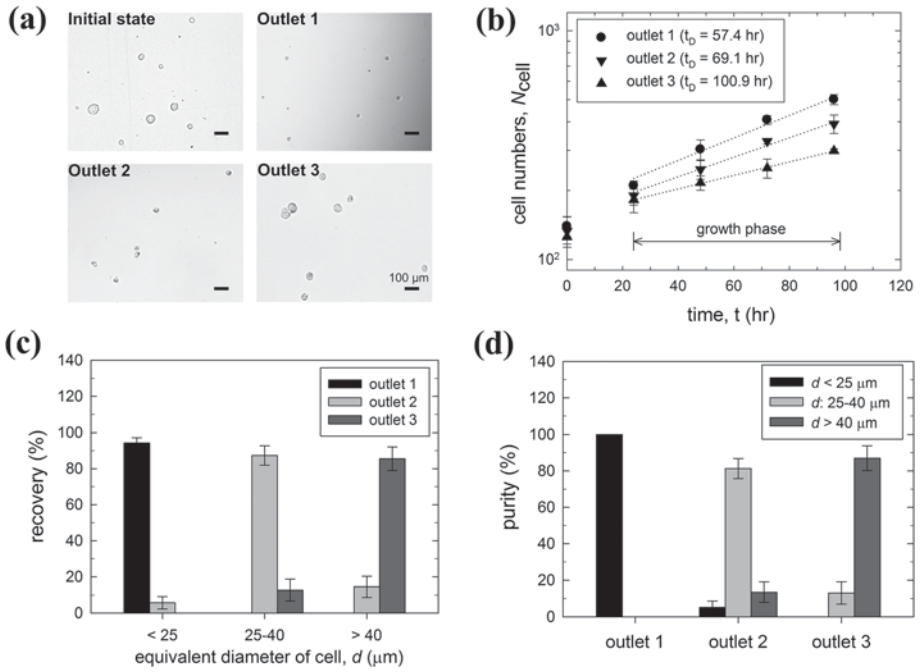


**Fig. 7** (a) Micrographs of hMSC suspensions before separation and after collection from each outlet, and (b) their cell growth behavior. Sorting results for hMSCs with (c) purity at each outlet and (d) recovery distribution of cells according to outlet. Each value shows the mean ± SE from three independent experiments.

large cell populations from hMSCs is possible to effectively concentrate the population of hMSCs with high multipotency.

We would like to point out that our result of the recovery and purity for hMSCs appears better compared with the previous results reported for blood cells and liver cells, but is slightly lower than the perfect efficiency of rigid particles, due to the effect of cell deformation.[29] According to the cut-off widths given as 12.5 μm for outlet 1 and 20 μm for outlet 2, populations of small, medium, and large cells would be recovered from outlets 1, 2, and 3, respectively. The deformation is so weak during HDF that our designed channel based on the center-of-mass of spherical cell can generally be applied to cell sorting. However, the center-of-mass of deformed cells is changed due to their indefinite shapes and rotation. Another issue is an effect of lateral migration with respect to the deformability, resulting in decreasing the strength of focusing, which should be examined for further study.

Note that the expression of each surface marker is one of the minimal criteria for defining hMSCs.[30] According to the previous report, while large FL cells do not have CD73 expression, small RS cells are shown to express CD73, CD90 and CD105.[6] In Fig. 8a, the small cells collected from outlet 1 showed the expression of both CD73 and CD90, indicating that they were RS-like cells. The medium-sized cells from outlet 2 were spindle-shaped and the large cells from outlet 3 did not show CD73 expression, indicating that they were SS-like and FL-like cells, respectively. In Fig. 8b, the cells collected from outlet 1 also showed high expression levels of CD73 and CD105, but the cells collected from outlet 3 did not show CD73 expression. In addition, we counted the number of cells expressing each surface marker and estimated the proportion of positive cells from each outlet. In Table 2, all the cells from outlet 1 were double positive for CD73/CD90, whereas most cells from outlet 3 (84.4%) were single positive for CD90. Similar results were obtained with double immunocytochemistry of CD73/CD105, where all the cells from outlet 1 were double positive, whereas most cells from outlet 3 (91.7%) were single positive for CD105.

We also measured the maximum diameter and the area of cells from each outlet (Fig. 8a and b). Our results are consistent with the previous report that the maximum diameter of RS cells is less than 157 μm and the area is smaller than 6617 $\mu m^2$, while FL cells have a larger maximum diameter (>157 μm) and a larger area (>6617 $\mu m^2$).[6] As in the previous report, the correlation is evident between the morphological characteristic of each subpopulation of hMSCs and the expression pattern of corresponding surface markers. These data suggest that sorting hMSCs using microfluidic chip filtration can successfully fractionate the three subpopulations RS, SS and FL cells, contributing to the improvement of the effectiveness of cell therapy.

## Conclusions

Since the hMSCs consist of heterogeneous populations based on the size and each subpopulation has significantly different multipotency, sorting out a certain subpopulation from the others in hMSCs is an important technique. We designed the chip by applying the optimum parameters rigorously deter-

 

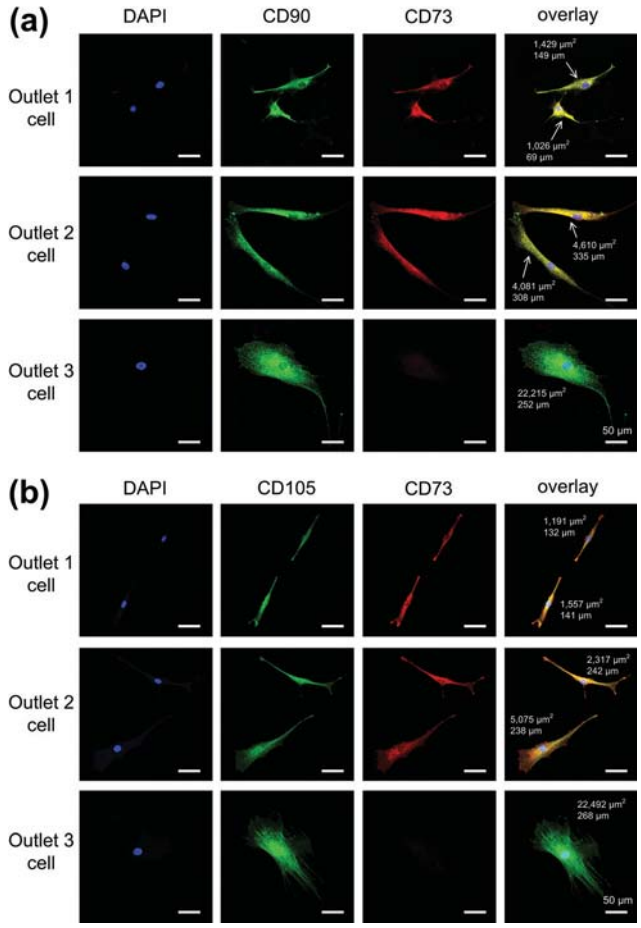


**Fig. 8** Morphological and immunocytochemical characterizations of hMSC subpopulations using immunocytochemistry. The images show the maximum diameter and area with the expressions of (a) CD73 and CD90; (b) CD73 and CD105 in each collected cell.

**Table 2** Immunocytochemical analysis of hMSC subpopulations

| | | No. of cells (%) | | |
|---|---|---|---|---|
| Surface marker | Total no. of cells | Outlet 1 | Outlet 2 | Outlet 3 |
| CD73(+) | 134 | 0 (0) | 3 (6.4) | 0 (0) |
| CD90(+) | | 0 (0) | 3 (6.4) | 27 (84.4) |
| CD73(+)/CD90(+) | | 55 (100) | 41 (87.2) | 0 (0) |
| CD73(−)/CD90(−) | | 0 (0) | 0 (0) | 5 (15.6) |
| CD73(+) | 183 | 0 (0) | 3 (4.4) | 0 (0) |
| CD105(+) | | 0 (0) | 3 (4.4) | 44 (91.7) |
| CD73(+)/CD105(+) | | 67 (100) | 62 (91.2) | 0 (0) |
| CD73(−)/CD105(−) | | 0 (0) | 0 (0) | 4 (8.3) |

mined by laminar flow theorem and hydraulic resistance in the multiple channel networks. The microfluidic chip has main, side, and 55 branch channels, where each channel is divided and connected to three outlets for trimodal separation of hMSCs as small, medium, and large groups. The viability and surface marker expressions of hMSCs collected from each outlet were examined to prove that our microfluidic chip could be applied to efficient sorting.

The recovery and purity of hMSCs estimated to validate our designed chip appeared to have better results compared with those previously reported for blood cells and liver cells. Although complete purity in small cells was achieved, sorting efficiency of deformable cells was slightly lower than the perfect efficiency of rigid particles. Thus, to improve the sorting efficiency of cells (especially medium and large cells), it is necessary to consider the more complicated effect of cell deformation in designing microfluidic chips.

## Acknowledgements

This work was supported by the Korean Health Technology R&D Project (grant no. A120476) from the Ministry of Health & Welfare and by the KIST Institutional Program (project no. 2E24812). The authors are grateful to S.-Y. Yu and M. Han for their help with the hMSC preparation and microchip fabrications. We also wish to thank the anonymous reviewers for their detailed and valuable comments to improve the manuscript.

## References

1 M. F. Pittenger, A. M. Mackay, S. C. Beck, R. K. Jaiswal, R. Douglas, J. D. Mosca, M. A. Moorman, D. W. Simonetti, S. Craig and D. R. Marshak, Multilineage potential of adult human mesenchymal stem cells, *Science*, 1999, **284**, 143–147.
2 D. G. Phinney and D. J. Prockop, Concise review: mesenchymal stem/multipotent stromal cells: the state of transdifferentiation and modes of tissue repair – current views, *Stem Cells*, 2007, **25**, 2896–2902.
3 L. S. Sherman, J. Munoz, S. A. Patel, M. A. Dave, I. Paige and P. Rameshwar, Moving from the laboratory bench to patients' bedside: considerations for effective therapy with stem cells, *Clin. Transl. Sci.*, 2011, **4**, 380–386.
4 D. C. Colter, I. Sekiya and D. J. Prockop, Identification of a subpopulation of rapidly self-renewing and multipotential adult stem cells in colonies of human marrow stromal cells, *Proc. Natl. Acad. Sci. U. S. A.*, 2001, **98**, 7841–7845.
5 J. R. Smith, R. Pochampally, A. Perry, S.-C. Hsu and D. J. Prockop, Isolation of a highly clonogenic and multipotential subfraction of adult stem cells from bone marrow stroma, *Stem Cells*, 2004, **22**, 823–831.
6 F. Haasters, W. C. Prall, D. Anz, C. Bourquin, C. Pautke, S. Endres, W. Mutschler, D. Docheva and M. Schieker, Morphological and immunocytochemical characteristics indicate the yield of early progenitors and represent a quality control for human mesenchymal stem cell culturing, *J. Anat.*, 2009, **214**, 759–767.
7 A. Lenshof and T. Laurell, Continuous separation of cells and particles in microfluidic systems, *Chem. Soc. Rev.*, 2010, **39**, 1203–1217.
8 H.-W. Wu, C.-C. Lin and G.-B. Lee, Stem cells in microfluidics, *Biomicrofluidics*, 2011, **5**, 13401.

9 E. L. Jackson and H. Lu, Advances in microfluidic cell separation and manipulation, *Curr. Opin. Chem. Eng.*, 2013, **2**, 398–404.

10 E. Primiceri, M. S. Chiriacò, R. Rinaldi and G. Maruccio, Cell chips as new tools for cell biology – results, perspectives and opportunities, *Lab Chip*, 2013, **13**, 3789–3802.

11 A. Y. Fu, C. Spence, A. Scherer, F. H. Arnold and S. R. Quake, A microfabricated fluorescence-activated cell sorter, *Nat. Biotechnol.*, 1999, **17**, 1109–1111.

12 J. Nilsson, M. Evander, B. Hammarstrom and T. Laurell, Review of cell and particle trapping in microfluidic systems, *Anal. Chim. Acta*, 2009, **649**, 141–157.

13 Y. Gao, W. Li and D. Pappas, Recent advances in microfluidic cell separations, *Analyst*, 2013, **138**, 4714–4721.

14 M. P. MacDonald, G. C. Spalding and K. Dholakia, Microfluidic sorting in an optical lattice, *Nature*, 2003, **426**, 421–424.

15 T. Schneider, S. Karl, L. R. Moore, J. J. Chalmers, P. S. Williams and M. Zborowski, Sequential CD34 cell fractionation by magnetophoresis in a magnetic dipole flow sorter, *Analyst*, 2010, **135**, 62–70.

16 K.-A. Hyun and H.-I. Jung, Microfluidic devices for the isolation of circulating rare cells: a focus on affinity-based, dielectrophoresis, and hydrophoresis, *Electrophoresis*, 2013, **34**, 1028–1041.

17 D. Di Carlo, D. Irimia, R. G. Tompkins and M. Toner, Continuous inertial focusing, ordering, and separation of particles in microchannels, *Proc. Natl. Acad. Sci. U. S. A.*, 2007, **104**, 18892–18897.

18 A. Aota, S. Takahashi, K. Mawatari, Y. Tanaka, Y. Sugii and T. Kitamori, Microchip-based plasma separation from whole blood via axial migration of blood cells, *Anal. Sci.*, 2011, **27**, 1173–1178.

19 T. Kawamata, M. Yamada, M. Yasuda and M. Seki, Continuous and precise particle separation by electroosmotic flow control in microfluidic devices, *Electrophoresis*, 2008, **29**, 1423–1430.

20 M. Yamada and M. Seki, Hydrodynamic filtration for on-chip particle concentration and classification utilizing microfluidics, *Lab Chip*, 2005, **5**, 1233–1239.

21 M. Yamada and M. Seki, Microfluidic particle sorter employing flow splitting and recombining, *Anal. Chem.*, 2006, **78**, 1357–1362.

22 M. Yamada, K. Kano, Y. Tsuda, J. Kobayashi, M. Yamato, M. Seki and T. Okano, Microfluidic devices for size-dependent separation of liver cells, *Biomed. Microdevices*, 2007, **9**, 637–645.

23 S. Sugaya, M. Yamada and M. Seki, Observation of non-spherical particle behaviors for continuous shape-based separation using hydrodynamic filtration, *Biomicrofluidics*, 2011, **5**, 024103.

24 H. Bruus, *Theoretical Microfluidics*, Oxford University Press, New York, 2008.

25 H. A. Stone, A. D. Stroock and A. Ajdari, Engineering flows in small devices: Microfluidics toward a Lab-on-a-Chip, *Annu. Rev. Fluid Mech.*, 2004, **36**, 381–411.

26 J. Abadie and J. Carpentier, Generalization of the Wolfe reduced gradient method to the case of nonlinear constraints, in *Optimization*, ed. R. Fletcher, Academic Press, London, 1969.

27 J. H. Yoo, D. H. Woo, M.-S. Chang and M.-S. Chun, Microfluidic based biosensing for Escherichia Coli detection by embedding antimicrobial peptide-labeled beads, *Sens. Actuators, B*, 2014, **191**, 211–218.

28 H.-W. Park, J.-S. Cho, C.-K. Park, S. J. Jung, C.-H. Park, S.-J. Lee, S. B. Oh, Y.-S. Park and M.-S. Chang, Directed induction of functional motor neuron-like cells from genetically engineered human mesenchymal stem cells, *PLoS One*, 2012, **7**, e35244.

29 T. M. Geislinger and T. Franke, Hydrodynamic lift of vesicles and red blood cells in flow - from Fåhræus & Lindqvist to microfluidic cell sorting, *Adv. Colloid Interface Sci.*, 2014, **208**, 161–176.

30 M. Dominici, K. Le Blanc, I. Mueller, I. Slaper-Cortenbach, F. C. Marini, D. S. Krause, R. J. Deans, A. Keating, D. J. Prockop and E. M. Horwitz, Minimal criteria for defining multipotent mesenchymal stromal cells. The International Society for Cellular Therapy position statement, *Cytotherapy*, 2006, **8**, 315–317.